Relaxor antiferroelectric ceramics with ultrahigh efficiency for

energy storage applications

Pratyasha Mohapatra, Zhongming Fan, Jun Cui, Xiaoli Tan*

Department of Materials Science and Engineering, Iowa State University, Ames, Iowa 50011, USA

*Author to whom correspondence should be addressed. Electronic mail: xtan@iastate.edu

Abstract

Enhancing the efficiency in energy storage capacitors minimizes energy dissipation and

improves device durability. A new efficiency-enhancement strategy for antiferroelectric

ceramics, imposing relaxor characteristics through forming solid solutions with relaxor

compounds, is demonstrated in the present work. Using the classic antiferroelectric

 $(Pb_{0.97}La_{0.02})(Zr_{1-x-v}Sn_xTi_v)O_3$ as model base compositions, $Bi(Zn_{2/3}Nb_{1/3})O_3$ is found to be most

effective in producing the "relaxor antiferroelectric" behavior and minimizing the electric

hysteresis. Specifically, a remarkable energy storage efficiency of 95.6% (with an energy density

of 2.19 J/cm³ at 115 kV/cm) is achieved in the solid solution

 $0.90(Pb_{0.97}La_{0.02})(Zr_{0.65}Sn_{0.30}Ti_{0.05})O_3-0.10Bi(Zn_{2/3}Nb_{1/3})O_3$. The validated new strategy, hence,

can guide the design of future relaxor antiferroelectric dielectrics for next generation energy

storage capacitors.

Keywords: Relaxor antiferroelectric, electric hysteresis, energy storage efficiency,

 $Bi(Zn_{2/3}Nb_{1/3})O_3$

1

1. Introduction

Antiferroelectric (AFE) materials are considered one of the most suitable dielectrics for high energy density capacitors [1-6]. They exhibit a nearly zero remanent polarization as compared to ferroelectric (FE) materials and a much higher permittivity as compared to linear dielectrics. The working mechanism for an AFE capacitor is through electric field-induced phase transitions. During charging, the AFE dielectric abruptly transforms to a FE state at a critical field E_F , and during discharging it reverts to the AFE state at E_A (Fig. 1a). The displacive and diffusionless nature of the AFE-FE phase transition engenders the extremely fast charge/discharge rate ($\sim 1 \mu s$) [7]. Therefore, AFE capacitors exhibit a high power density as well, in addition to their high energy density [1,2,5].

PbZrO₃ is the prototype AFE compound. Even though its complex crystal structure has been extensively investigated, its AFE-FE phase transition is rarely reported [8] due to the fact that at room temperature its E_F is higher than its breakdown strength. Many different composition systems have, thus, been developed by chemically modifying PbZrO₃ with La, Nb, Sn, and Ti to reduce the E_F , facilitate the sintering process, and improve the energy storage performance [9-13]. However, the existence of an electric hysteresis ($\Delta E = E_F - E_A$) of the AFE-FE phase transition indicates that the recovered energy (W_{re}) during discharging is considerably less than the stored energy (W_{st}) during charging. This has limited the energy efficiency η , defined as the ratio of W_{re}/W_{st} , in the range of 65 ~ 80 % for PbZrO₃-based AFE ceramics. Early attempts on reducing ΔE by substituting Pb with Ba or Sr have resulted in improvements of the energy efficiency η , but it still remained below 85% [14,15].

It is known that relaxor ferroelectrics exhibit a slim polarization-field (P-E) loop (Fig. 1b), meaning a nearly zero hysteresis. Classic relaxor compounds are complex perovskite oxides, such as Pb(Mg_{1/3}Nb_{2/3})O₃ and Pb(Zn_{1/3}Nb_{2/3})O₃, with cations of different valences sharing the same sublattice [16,17]. The random occupancy of these cations on the sharing sublattice randomizes local fields and disrupts long range dipole order, leading to the formation of nanoscale FE domains (polar nanoregions) [17]. Adding a relaxor compound, such as Pb(Mg_{1/3}Nb_{2/3})O₃, to a normal FE, such as PbTiO₃, has shown to impose relaxor characteristics to the solid solution with a much reduced hysteresis [16]. On the similar line, if the AFE long range order is disrupted by introducing relaxor characteristics, slim P-E loops with reduced ΔE may also be possible (Fig. 1c) [18]. Disrupted AFE order in the form of nanoscale AFE domains was indeed observed and the concept of "relaxor antiferroelectric" was proposed in 2010 [19]. This concept has been explored to manipulate the AFE-FE phase transition by single element doping (Ba, Al, Bi, or La) and apparent reduction in ΔE has been realized successfully in various solid solutions systems [20-24].

However, incorporation of a complex perovskite compound into PbZrO₃-based AFE compositions to introduce relaxor characteristics for reduced ΔE has not yet been explored. In the present work, (Pb_{0.97}La_{0.02})(Zr_{0.66}Sn_{0.27}Ti_{0.07})O₃ (abbreviated as PLZST 27/7/2), a typical AFE composition reported previously [25], is selected to make solid solutions with three complex perovskites Bi(Zn_{1/2}Ti_{1/2})O₃ (BZT), Bi(Zn_{2/3}Nb_{1/3})O₃ (BZN), and Bi(Zn_{3/4}W_{1/4})O₃ (BZW) in order to realize relaxor antiferroelectric ceramics. These relaxor compounds are selected for three reasons. First, they will introduce cations of different valences to both A- and B-site on the ABO₃ crystal lattice, which is expected to promote the relaxor behavior. Second, Bi³⁺ on the A-site and Zn²⁺, Ti⁴⁺, Nb⁵⁺ and W⁶⁺ on the B-site will help to produce a high polarization in the induced FE phase [26-30], which is needed for a high energy storage density. Third, it has been reported that

adding these complex compounds to BaTiO₃ disrupts the long-range FE order and leads to strong relaxor characteristics [31-33]. Presumably, these compounds could disrupt the long-range AFE order in PbZrO₃-based ceramics. Figure 1 schematically illustrates the rational for the present experimental work: reducing electric hysteresis ΔE by realizing the relaxor AFE behavior.

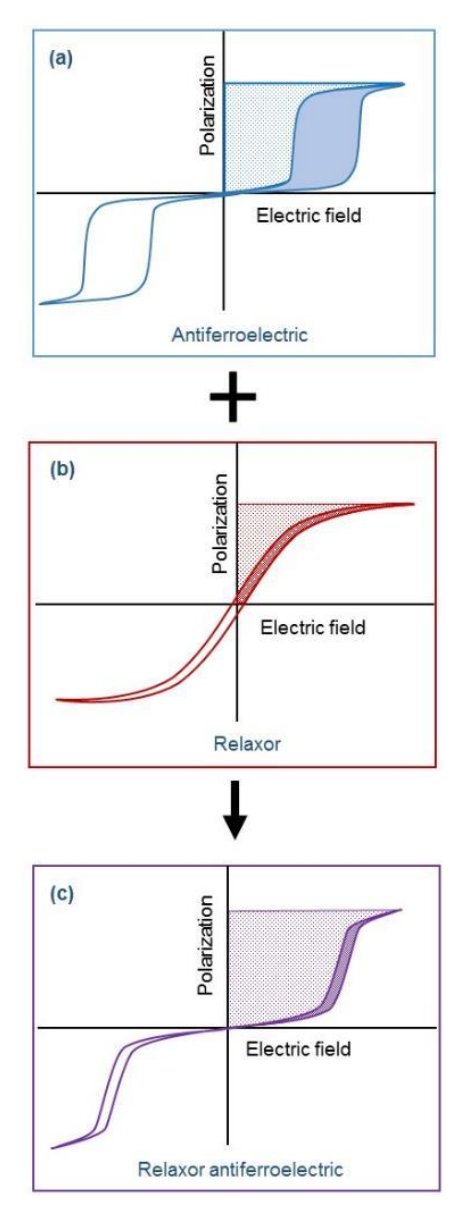


Fig. 1 Schematic representation of polarization - electric field (*P-E*) hysteresis loop characteristics of relaxor modification to antiferroelectric materials: (a) Antiferroelectric material, (b) relaxor material, and (c) relaxor modified antiferroelectric material.

2. Experimental

The AFE ceramic of $(Pb_{0.97}La_{0.02})(Zr_{0.66}Sn_{0.27}Ti_{0.07})O_3$, abbreviated as PLZST 27/7/2, and its solid solutions of $0.90[(Pb_{0.97}La_{0.02})(Zr_{0.66}Sn_{0.27}Ti_{0.07})O_3]-0.10[Bi(Zn_{1/2}Ti_{1/2})O_3],$ $0.90[(Pb_{0.97}La_{0.02})(Zr_{0.66}Sn_{0.27}Ti_{0.07})O_3]-0.10[Bi(Zn_{2/3}Nb_{1/3})O_3],$ and $0.90[(Pb_{0.97}La_{0.02})(Zr_{0.66}Sn_{0.27}Ti_{0.07})O_3]-0.10[Bi(Zn_{3/4}W_{1/4})O_3]$ (abbreviated as PLZST-10BZT, PLZST-10BZN, and PLZST-10BZW, respectively), are prepared with the solid state reaction process. The content of the relaxor compounds is determined based on the fact that 10 mol.% is the solubility limit of BZT in PbZrO₃ [29]. High purity powders (> 99.9%) of PbO, La₂O₃, ZrO₂, SnO₂, TiO₂, Bi₂O₃, ZnO, Nb₂O₅ and WO₃ are batched in stoichiometric quantities. An excess of 3 wt.% PbO is included to account for the lead loss due to evaporation in the subsequent thermal processing steps. The powders are mixed with ethanol and milled for 6 hours. The milled slurry is dried overnight to evaporate the ethanol solvent. The dried mixture is then calcined at 935 °C for 4 hours. The calcined product is milled and dried again. Then, the powder is mixed with a 10 wt.% polyvinyl alcohol binder and uniaxially pressed into 10 mm diameter pellets. The pellets are sintered in a lead-rich environment using a double crucible arrangement, to minimize lead loss during sintering. The binder is burned out at 600 °C for 3 hours and the pellets are sintered at different temperatures ranging from 1300 °C to 1360 °C for 3 hours depending on the composition.

The sintered pellets are mechanically polished to remove surface layers, then annealed above the Curie temperature to minimize the residual stresses. X-ray diffraction (Siemens D500) is carried out with a Cu source in the 2 theta range of 20°-70°, to determine the crystal structure and phase purity. Relative densities of the sintered ceramics are calculated using the Archimedes principle. The grain size and morphology are examined using scanning electron microscopy (SEM) on the fractured surface of the sintered pellets. In order to reveal the grain boundaries, the samples

are thermally etched at 1150°C for 30 minutes. The domain structure characteristics within grains are analyzed using transmission electron microscopy (TEM, FEI Tecnai G2-F20). The TEM specimen preparation follows the procedure in the sequence of disk cutting, dimpling, polishing, annealing, and Ar-ion milling. For electrical property measurements, silver electrodes are sputtered on both flat faces of the polished and annealed pellets. The dielectric property measurement of the samples is conducted at frequencies of 1kHz, 10kHz, and 100kHz with an LCR meter (HP-4284A, Hewlett-Packard) while heating the samples at a rate of 4 °C/min. The polarization response to applied electric field is measured at room temperature at 1 Hz frequency, using a standardized ferroelectric test system (Precision LC II, Radiant Technologies). For this measurement, disk samples of a thickness around 0.3 mm with both electrodes of a diameter of 4 mm are used.

3. Results

3.1. Structure of the solid solution ceramics

X-ray diffraction patterns of PLZST 27/7/2 and its solid solutions, shown in Fig. 2, display distorted perovskite structures. No peaks of pyrochlore or other impurity phases are visible in any of the compositions, confirming that the ceramics are phase pure. The peaks are indexed according to the pseudo-cubic unit cell. All the compositions show a tetragonal distortion as can be seen from the splitting of the (200) pseudo-cubic peak, which is closely examined in Fig. 2b. The addition of 10 mol.% BZT shows a small reduction in the crystal lattice volume as the peaks slightly shift to high angles. The change in the crystal lattice is expected as ions with smaller radii are introduced into the lattice. On the other hand, addition of both 10 mol.% BZN and 10 mol.% BZW shift the peaks to lower Bragg angles, indicating an increase in the cell volume. This increase can be

attributed to the increase in the average radius of B-site cation on the introduction of larger Zn^{2+} (0.74 Å), even though smaller size Bi^{3+} (1.35 Å) ions are simultaneously introduced in the A-site [30,34,35].

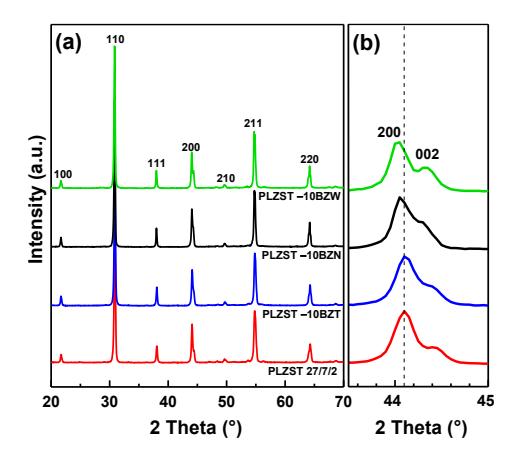


Fig. 2 X-ray diffraction spectra of sintered (Pb_{0.97}La_{0.02})(Zr_{0.66}Sn_{0.27}Ti_{0.07})O₃ ceramic and its solid solutions. (a) Full spectra in the 2θ range of 20°-70°, (b) the enlarged (200) pseudo-cubic peak.

Table 1 summarizes the crystal structure data of the base PLZST 27/7/2 composition and its solid solutions. It is noted that in BZN addition, the increase in unit cell volume is accompanied by a change of the tetragonality towards unity. In the BZW modified composition, the splitting of the (200) and (002) peak is more prominent than that of BZN modification, corresponding to a lattice distortion close to that of the base composition. The results indicate that Bi-based complex perovskites dissolve into the PLZST 27/7/2 base AFE composition and have changed its lattice structure, and BZN addition has reduced the lattice distortion.

Table 1 Crystal structure and energy storage properties of the antiferroelectric ceramics

Campacition	Crystal structure				Energy storage properties*		
Composition	a (Å) c (Å) V (Å ³) c/a W_{re} (J/cm ³)	$W_{\rm re}$ (J/cm ³)	$\Delta E (kV/cm)$	η (%)			
PLZST 27/7/2	4.114	4.082	69.088	0.992	1.95	18.1	82.6
PLZST-10BZT	4.112	4.086	69.088	0.994	0.75	21.0	52.1
PLZST-10BZN	4.115	4.094	69.325	0.995	1.76	4.7	93.2
PLZST-10BZW	4.117	4.090	69.324	0.993	2.20	16.9	83.9

^{*} Properties are evaluated at the peak field of 100, 80, 100, 120 kV/cm for PLZST 27/7/2, PLZST-10BZT, PLZST-10BZN, PLZST-10BZW, respectively.

Figure 3 shows the SEM micrographs of the fracture surface of sintered PLZST 27/7/2 and its solid solutions. The sintered ceramics are fractured, then thermally etched at 1150 °C for 30 mins to facilitate SEM imaging of the grain boundaries. The average grain size is calculated with the linear intercept method. The grain size is determined to be 4.77 μm for PLZST 27/7/2, 3.02 μm for PLZST–10BZT, 3.22 μm for PLZST–10BZN, and 3.40 μm for PLZST–10BZW, respectively. The incorporation of multivalent ions into the base composition seems to inhibit the growth of the grains as reduction in the grain size is observed on relaxor compound addition. The other distinctive feature is the change in fracture mode of the ceramics. The base composition ceramic shows a transgranular fracture mode in contrast to the intergranular fracture in all the relaxor modified compositions. The larger grain size of the PLZST 27/7/2 base composition appears to promote the transgranular fracture compared to the smaller grains in the doped compositions [36]. In addition, the sintering conditions used result in high relative densities in all the ceramic pellets, calculated to be 94%, 96%, 96% and 98% for PLZST27/7/2, PLZST–10BZT, PLZST–10BZN, and PLZST–10BZW, respectively.

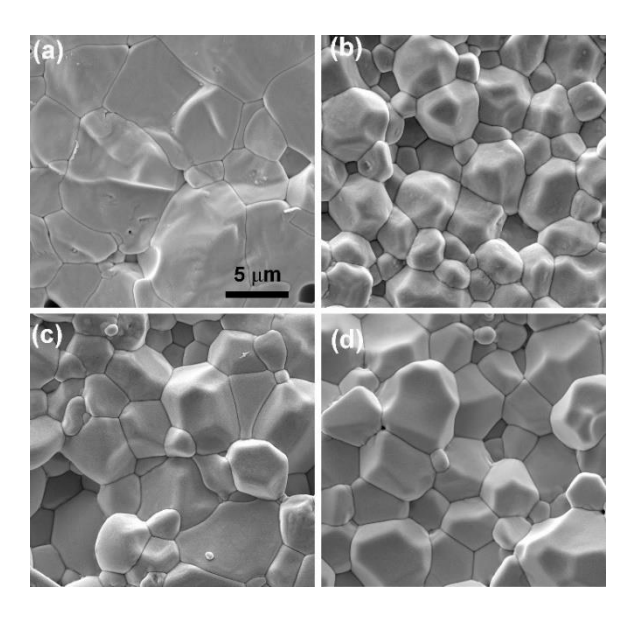


Fig. 3 SEM micrographs of the fracture surface of (a) PLZST27/7/2, (b) PLZST-10BZT, (c) PLZST-10BZN, and (d) PLZST-10BZW. The scale bar in (a) also applies to (b), (c), (d).

The domain structure in all four compositions are analyzed with TEM. In the base composition PLZST 27/7/2, the grain is dominantly occupied by the checkerboard-like pattern consisting of alternatively bright and dark AFE domains (Fig. 4a). The inset shows the selected area electron diffraction (SAED) pattern recorded across the domain wall, in which the two perpendicular sets of satellite diffraction spots indicate the incommensurate modulations in the two neighboring AFE domains [9,20]. Also, a spindle-shaped FE domain is observed to be embedded in a large bright AFE domain. This is not surprising as the presence of minor FE phase is quite common in AFE perovskites [37]. However, the volume fraction of the FE phase is obviously increased in PLZST-10BZT where AFE and FE domains are found overlapping with each other in the major portion of the grain (Fig. 4b). The SAED patterns recorded from nonoverlapping AFE (with satellites) and FE (without satellites) regions are displayed in the insets. With BZN modification, on the other hand, the size of AFE domains and the fraction of the minor FE phase appear similar to those in the base composition (Fig. 4c). However, the diffraction contrast of the checkerboard pattern appears significantly weaker under the same imaging conditions, which might indicate a smaller strain field/lattice distortion in PLZST-10BZN. In PLZST-10BZW, the domain structure does not resemble to any of the other three compositions (Fig. 4d). The AFE domains are considerably smaller in size, giving rise to a much denser morphology of AFE domains than the base composition PLZST 27/7/2. In addition, no FE domains are observed in PLZST-10BZW.

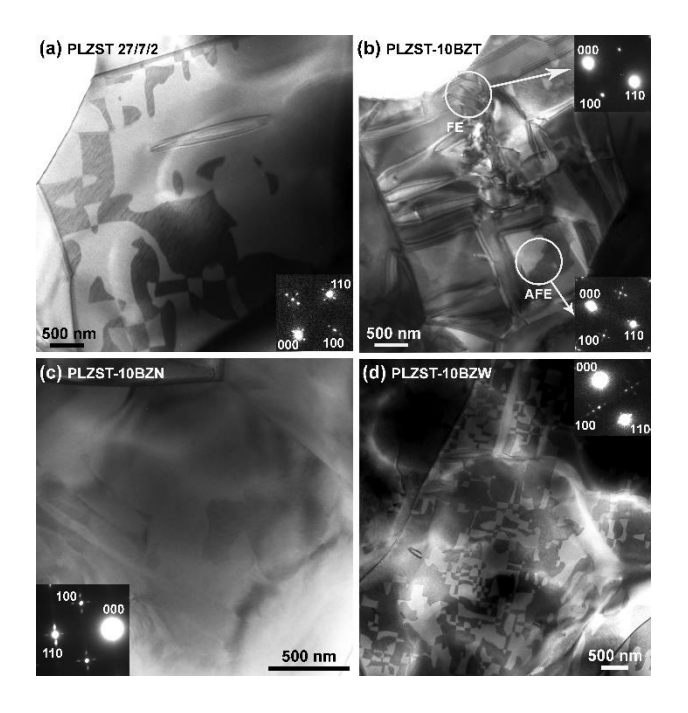


Fig. 4 TEM micrographs of (a) PLZST27/7/2, (b) PLZST-10BZT, (c) PLZST-10BZN, and (d) PLZST-10BZW. Insets are SAED patterns recorded across the AFE domain wall in (a), (c) and (d), and indicated regions in (b).

3.2. Electrical properties of the solid solution ceramics

The dependence of the dielectric constant, ε_r , of the ceramics on temperature at different frequencies is presented in Fig. 5a. The dielectric loss tangent, $\tan \delta$, of the ceramics as a function of temperature is shown in Fig. 5b. The plots are presented on the same scale for different compositions for easy direct comparison. The dielectric constant in PLZST 27/7/2 increases till 166 °C which is followed by a plateau region till 194 °C and drops thereafter. The AFE phase is considered to be stable below 166 °C. The plateau region was suggested to correspond to a multicell cubic phase that is present between the AFE and the paraelectric simple cubic phase. The presence of this multicell cubic phase has been attributed to Sn in the composition that tends to disrupt the AFE transformation [38]. No apparent frequency dispersion is observed in the AFE region in the base composition.

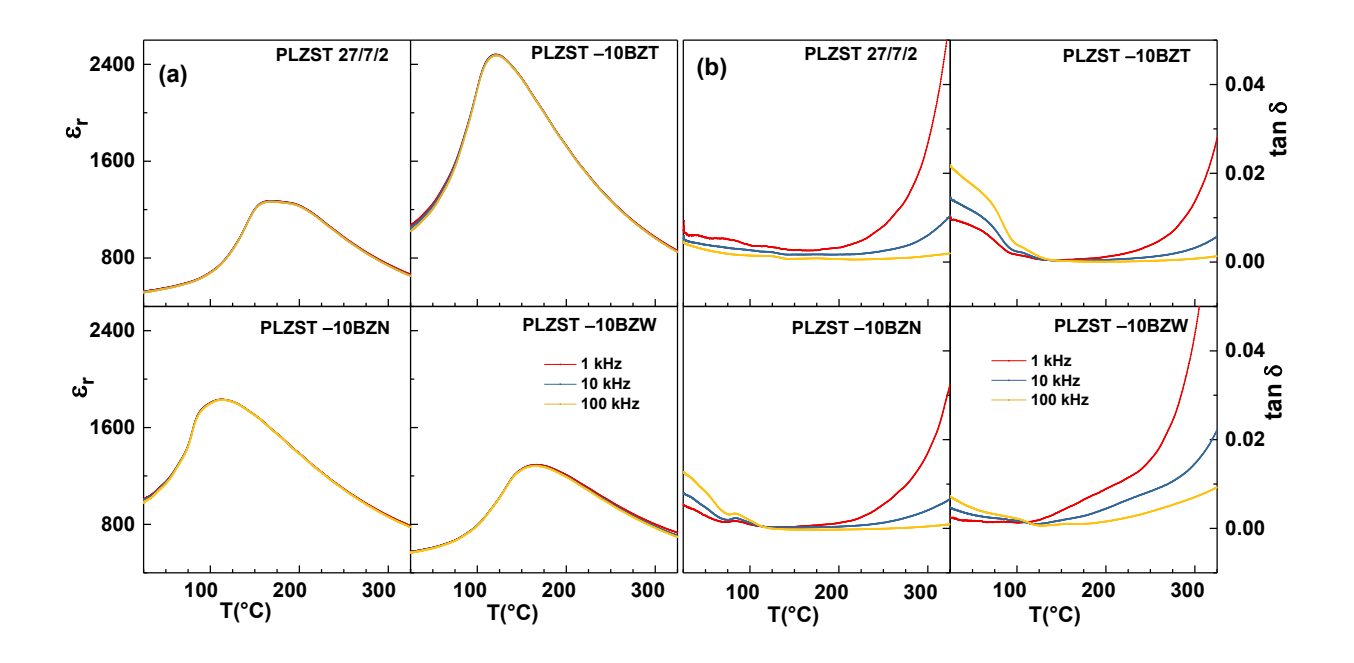


Fig. 5 (a) The dielectric constant, ε_r , of PLZST 27/7/2 and its solid solutions, as a function of temperature during heating. (b) Dielectric loss tangent, $\tan \delta$, of all the ceramics during heating.

The addition of BZT to the base composition PLZST 27/7/2 almost doubles the maximum dielectric constant ($\varepsilon_{m,r}$) value but also lowers the temperature of dielectric maxima (T_m) to 121° C. This decrease in T_m and increase in $\varepsilon_{m,r}$ is similar to that observed in previous studies on addition of BZT to PbZrO₃ [29]. The frequency dispersion of the dielectric constant increases at lower temperatures, in the AFE stable region, and the dispersion at T_m is very low but T_m increases with increasing frequency. This can be attributed to the introduction of relaxor dielectric behavior to the base composition by incorporation of BZT. The frequency dispersion is more prominent in the dielectric loss plot in Fig. 5b. The loss tangent is higher for higher frequencies in the AFE region and decreases to a minimum at the T_m and then increases again at higher temperatures. This is a characteristic feature of relaxor behavior [16,17] and is in contrast to the base composition where the dielectric loss is higher for lower frequencies. When BZN is added to PLZST 27/7/2, the

dielectric constant increases, and $T_{\rm m}$ shifts down to 113 °C. A similar effect of decrease in $T_{\rm m}$ was also seen on BZN addition to ferroelectric Pb(Mg_{1/3}Nb_{2/3})O₃–PbTiO₃ [34]. Frequency dispersion in the dielectric constant and the loss tangent is also observed. The dielectric loss is lower than that of PLZST–10BZT around room temperature in the AFE region but the dispersion is much stronger than the base composition PLZST 27/7/2, confirming the relaxor behavior imposed by BZN modification. Addition of BZW to PLZST does not show apparent change in the dielectric constant and $T_{\rm m}$ remains at 166 °C. The frequency dispersion is not obvious in the dielectric constant plot, but the loss tangent plot does show an enhanced frequency dispersion compared to the base composition. It is evident that all three modifying compounds dramatically increase the frequency dispersion of dielectric permittivity around room temperature and successfully introduce relaxor characteristics to the AFE phase.

Apart from the frequency dispersion, another characteristic that is affected by the chemical modification is the plateau region of the dielectric constant curve in the base composition PLZST 27/7/2. The plateau seems to be eliminated after relaxor modification, indicating that the intermediate multicell cubic phase is no longer stable.

The polarization and energy storage properties are studied by plotting the P-E hysteresis loops for all the compositions. Figure 6 shows the results, where all the compositions display the characteristic double hysteresis loops. This is expected from the AFE microstructures revealed by TEM analysis. The application of electric field leads to an AFE to FE phase transition at E_F , manifesting itself as the abrupt increase in the polarization which saturates upon completion of the transition. The removal of the electric field then restores the AFE phase at E_A and the polarization drops to zero at 0 kV/cm. In the process of charging, as the polarization increases, energy is stored;

and is recovered as useful energy when electric field is removed during discharging. The energy storage characteristics are calculated as:

$$W_{\rm st} = \int_{P_{\rm r}}^{P_{\rm max}} E dP \tag{1}$$

$$W_{\rm re} = -\int_{P_{\rm max}}^{P_{\rm r}} E dP \tag{2}$$

where $W_{\rm st}$ is the energy stored during charging, $W_{\rm re}$ is the useful energy recovered, $P_{\rm r}$ is the remanent polarization, $P_{\rm max}$ is the maximum polarization at the peak field, and E is the applied electric field. The hysteretic energy loss is given by $W_{\rm loss} = W_{\rm st}$ - $W_{\rm re}$, and the energy efficiency (η) refers to the ratio of $W_{\rm re}/W_{\rm st}$. A high efficiency is desired in order to minimize energy loss and detrimental effects like overheating.

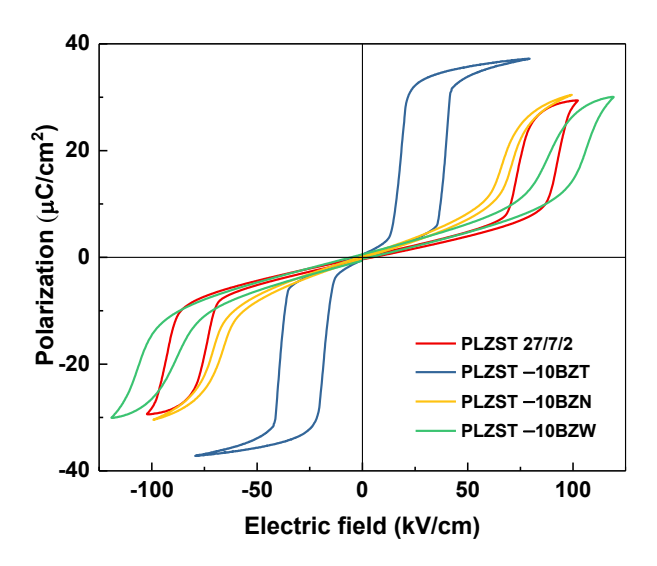


Fig. 6 Polarization vs. electric field hysteresis loops of PLZST 27/7/2 and its solid solutions measured at 1 Hz at room temperature.

The summary of the energy storage properties of all the four compositions are listed in Table 1. The base composition PLZST 27/7/2 has the critical field E_F at 87.2 kV/cm with an electric

hysteresis ΔE of 18.1 kV/cm. At a peak field of 100 kV/cm, $W_{\rm re}$ is measured to be 1.95 J/cm³ with an efficiency η of 82.6%. It can be seen that the addition of BZT reduces $E_{\rm F}$ to 35.4 kV/cm while considerably increases the maximum polarization value. The reduction in $E_{\rm F}$ was also observed by Khamman *et al.* [29] in BZT modified PbZrO₃ ceramics. The increase in $P_{\rm max}$ and decrease in $E_{\rm F}$ in PLZST–10BZT is in line with the presence of increased fraction of FE domains revealed by the TEM analysis. The significant decrease in $E_{\rm A}$ leads to a much reduced $W_{\rm re}$, and the enlarged ΔE contributes to a very low η .

The addition of BZN also reduces both $E_{\rm F}$ and $E_{\rm A}$ and increases $P_{\rm max}$, but the reduction in critical fields is not as severe as in PLZST-10BZT. Moreover, the AFE-FE transition becomes more diffuse (occurs within a wider range of electric field) compared to the base composition PLZST 27/7/2. It is interesting to observe that the P-E loop appears to be a hybrid of the classic AFE double hysteresis loops and the slim relaxor P-E loop. The electric hysteresis ΔE of this relaxor AFE is dramatically reduced to 4.7kV/cm from 18.1kV/cm in the base composition. With the reduction of the electric hysteresis, the energy efficiency of PLZST-10BZN reaches a remarkable value of 93.2% at a recoverable energy density of 1.76 J/cm³ (evaluated at a moderate field of 100 kV/cm). In the meantime, the hysteretic energy loss is suppressed to 0.12 J/cm³ from 0.34 J/cm³ in PLZST 27/7/2.

In contrast, BZW addition to PLZST 27/7/2 is seen to increase both $E_{\rm F}$ and $E_{\rm A}$, indicating a higher stability of the AFE phase. The AFE-FE phase transition also becomes diffuse, compared to the base composition. The simultaneous increase in $E_{\rm A}$ and $P_{\rm max}$ results in an increase in the recoverable energy density to 2.20 J/cm³ and the efficiency gets a small increase to 83.9%.

4. Discussion

4.1. Tolerance factor, electronegativity difference, and antiferroelectricity

The dielectric property and the AFE-FE phase transition behavior of the relaxor AFE compositions designed here can be understood better by examining the underlying structure. The stability of the ABO₃ perovskite structure, the polar ordering and, in turn, the trend of its properties have been shown to be affected largely by the tolerance factor (t), average electronegativity difference (X), and polarizability [39,40]. The tolerance factor is calculated as:

$$t = \frac{(R_A + R_O)}{\sqrt{2}(R_B + R_O)} \tag{3}$$

where R_A , R_B , and R_O are the ionic radii of the A- and B-site cations, and O anion, respectively. High values of t indicate stability of the perovskite structure and t > 1 correlates with the FE order. A low value of t below unity typically favors an AFE structure. The average electronegativity difference is given by:

$$X = \frac{(X_{AO} + X_{BO})}{2} \tag{4}$$

where X_{AO} and X_{BO} are the electronegativity difference between the A-site cation and oxygen and the B-site cation and oxygen. Previous works suggest that reducing both the tolerance factor t and the average electronegativity difference X favors antipolar ordering [39,41]. The tolerance factor values of all the compositions studied in the present work are calculated using the Shannon radii [35] and are presented in Table 2. It is seen that the tolerance factor is less than unity in all four compositions, consistent with the observed AFE order. Upon incorporation of BZT, BZN, and BZW into the base composition, the tolerance factor is reduced and deviates further away from unity. This is because Bi³⁺ (1.34Å) is smaller than Pb²⁺ (1.49Å) on the A-site while Zn²⁺ (0.74Å) is larger than Zr⁴⁺ and Sn⁴⁺ on the B-site. In the three modified compositions, the tolerance factor

appears to correlate well with the stability of the AFE phase indicated by E_F : PLZST-10BZT has a higher t value and a less stable AFE order than PLZST-10BZN and PLZST-10BZW.

Table 2 Tolerance factor t, average electronegativity difference X, and relaxor properties (γ, δ) of the studied AFE ceramics.

Composition	t	X	γ	δ
PLZST 27/7/2	0.965	1.845	1.36	21.10
PLZST-10BZT	0.962	1.838	1.56	33.07
PLZST-10BZN	0.961	1.836	1.65	51.81
PLZST-10BZW	0.961	1.834	1.58	44.61

In previous studies on AFE perovskite oxides [39-41], the impact of the electronegativity difference on the stability of AFE order was discussed. The average electronegativity difference of the compositions in the present study is also calculated using Pauling's values [42] and listed in Table 2. It shows that X decreases with relaxor modification and has a similar trend as the tolerance factor. In the three relaxor antiferroelectric compositions, X is the highest in PLZST-10BZT and the lowest in PLZST-10BZW. This trend, again, suggests that BZW addition most effectively stabilizes the AFE order, which is consistent with the highest E_F observed.

Though there seems to be a correlation between the tolerance factor t, the average electronegativity difference X, and the stability of AFE phase in the three modified relaxor AFE compositions, the base composition PLZST 27/7/2 does not lie in the same trend. The critical field E_F of the BZT and BZN modified compositions is lower than the base composition even though they have smaller t and X. The discrepancy suggests that there may be other influencing factors. It is noted that both Z_{1}^{2+} and Z_{2}^{4+} are strongly ferroelectric active B-site cations, Z_{2}^{5+} is moderately while Z_{2}^{6+} is weakly ferroelectric active cations [27]. Such aspect may affect the stabilization of

dipole ordering in the relaxor AFE compositions. This also possibly contributes to the enhanced P_{max} in all relaxor modified compositions.

4.2. Relaxor characteristics

It should be made clear that the main purpose of adding BZT, BZN and BZW to PLZST 27/7/2 is to impose relaxor characteristics by introducing cations of different valences to the lattices sites. In the base composition, all B-site cations are of 4+ valence (Zr⁴⁺, Sn⁴⁺, Ti⁴⁺), which are electrostatically balanced by the A-site Pb²⁺ cation. In a prime cell of such ABO₃ lattice, the cell will effectively carry -2e charges when the 4+ cation is substituted by Zn²⁺, +1e by Nb⁵⁺ substitution, and +2e by W⁶⁺ substitution. These effective charges can give rise to electric dipoles across prime cells on top of those already exist within prime cell due to lattice distortion or cation displacement [43]. The random occupancy of these cations of different valences randomizes the inter-prime-cell dipoles, resulting in the relaxor behavior. Furthermore, the complex interactions between these inter-cell dipoles and those within prime cells produce a subtle balance between the AFE and FE orders.

The relaxor characteristics introduced by BZT, BZN and BZW modification can be quantified by fitting the dielectric constant data above $T_{\rm m}$ to the equation [44,45]:

$$\frac{\varepsilon_{m,r}}{\varepsilon_r} = 1 + \frac{(T - T_m)^{\gamma}}{2\delta^2} \tag{5}$$

where the parameter γ indicates the degree of dielectric relaxation and δ (this symbol is not the phase angle in loss tangent tan δ) represents the diffuseness of the phase transition at $T_{\rm m}$. It can be seen that at $\gamma = 1$, Equation (5) represents the Curie-Weiss law for a first order ferroelectric transition; at $\gamma = 2$, the equation denotes a prototypical relaxor behavior. As the value of γ increases

from 1, the dielectric relaxation strengthens toward a greater relaxor behavior. Also a higher value of δ indicates a more diffuse phase transition and enhanced relaxor characteristic. For the four studied compositions, the $(\varepsilon_{\rm m,r}/\varepsilon_{\rm r})$ -1 vs. $T_{\rm m}$ -T data at 1 kHz are plotted in Fig. 7, in logarithmic scale.

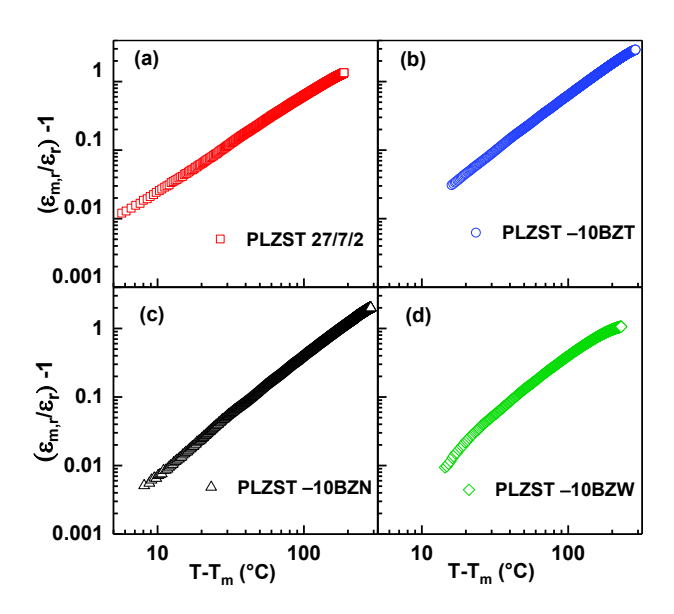


Fig. 7 The 1 kHz data displayed in Fig. 5 are replotted as $(\varepsilon_{\text{m,r}}/\varepsilon_{\text{r}})$ -1 vs. $(T-T_{\text{m}})$ in the log scale for (a) PLZST 27/7/2, (b) PLZST-10BZT, (c) PLZST-10BZN, (d) PLZST-10BZW.

The values of γ and δ are calculated from the slope and intercept of these plots and are presented also in Table 2. It is observed that the γ and δ values of PLZST 27/7/2 are the lowest, indicating the presence of long-range dipole order. With the incorporation of the relaxor doping compounds, both γ and δ increase, quantitatively confirming the enhanced relaxor behavior [46]. Of the four studied compositions, PLZST-10BZN displays the highest γ and δ ; hence, the most prominent relaxor behavior. This observation correlates extremely well with the lowest electric hysteresis ΔE of its narrow P-E loop (Fig. 6). These results justify that the concept of relaxor AFE

can indeed be exploited to design new AFE compositions with nearly zero electric hysteresis and ultrahigh energy efficiency.

It should be pointed out that PLZST-10BZN, with the highest γ , δ and the lowest ΔE , still displays AFE domains of similar size as in the base composition (Fig. 4). There is apparent reduction in the domain size in PLZST-10BZW, but its electric hysteresis ΔE is not at minimum. This suggests that there are multiple competing factors defining the final properties of these relaxor modified compositions. The X-ray structure analysis reveals that BZN addition leads to a tetragonality close to unity (Table 1), indicating a reduced lattice distortion which is in line with the low contrast in the TEM micrograph (Fig. 4). The reduced lattice distortion in PLZST-10BZN may help the kinetics of the AFE-FE displacive phase transition to realize a small hysteresis, similar to the displacive transition in thermoelastic alloys [47].

4.3. Relaxor antiferroelectrics with ultrahigh energy storage performance

Even though PLZST-10BZN displays a significantly enhanced energy storage efficiency, there is still room for improvement in terms of energy storage density. To confirm that BZN addition is also effective in reducing ΔE in other PbZrO₃-based compositions and verify the energy density can be further increased, BZN modification is applied to $(Pb_{0.97}La_{0.02})(Zr_{0.65}Sn_{0.30}Ti_{0.05})O_3$ (PLZST 30/5/2), another AFE base composition with a higher E_F . Figure 8 shows the P-E loops of PLZST 30/5/2 and PLZST 30/5/2-10BZN; the presence of apparent inflection points on the P-E loop of the modified composition confirms the occurrence of the AFE-FE phase transition. The results are very encouraging: An even lower ΔE (3.4 kV/cm), an increased energy density of 2.19

J/cm³, and a remarkable energy efficiency of 95.6% are achieved in the relaxor AFE PLZST 30/5/2–10BZN.

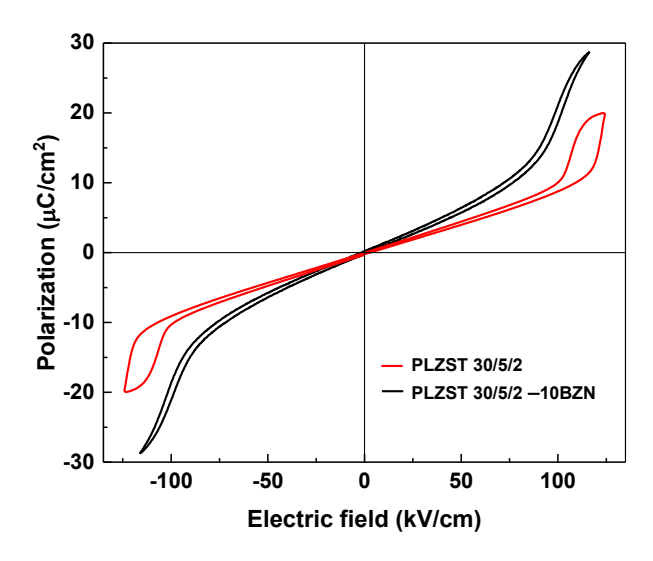


Fig. 8 Polarization vs. electric field hysteresis loops of PLZST 30/5/2 and PLZST 30/5/2–10BZN measured at 1 Hz at room temperature.

To put this remarkable energy efficiency into context, Table 3 lists η of some PbZrO₃-based, as well as a couple of lead-free, AFE compositions reported in recent literature. It can be seen that η in most lead-containing and lead-free perovskite AFE compositions lies in the range of 60~80% mainly due to the electric hysteresis of the AFE-FE phase transition. Such a moderate η implies that heat will be generated during high frequency applications which will adversely affect the device reliability and service lifetime. Although efficiencies above 90% are reported in the literature [22,23], those *P-E* curves are almost linear without any inflection points, indicating the linear dielectric behavior and the absence of the AFE-FE phase transition. Compared to all the energy efficiencies previously reported in AFE compositions, the PLZST 30/5/2–10%BZN in the present work exhibits the highest value (95.6%); at the same time, with an excellent energy density

of 2.19 J/cm³ at a moderate field of 115 kV/cm. It is expected that even higher values of energy density (> 5 J/cm³) can be achieved in other BZN-modified relaxor AFE compositions while maintaining the remarkable energy efficiency (> 95%).

Table 3 Comparison of the efficiency for energy storage using antiferroelectric ceramics

Composition	Energy efficiency η (%)	Reference
PLZST 27/7/2–10BZN	93.2	This work
PLZST 30/5/2-10BZN	95.6	This work
$Pb[(Lu_{0.5}Nb_{0.5})_{0.97}(Mg_{0.5}W_{0.5})_{0.03}]O_{3}$	72.7	[48]
$(Pb_{0.965}La_{0.035})(Zr_{0.9}Ti_{0.1})_{0.99125}O_{3}$	65.0	[49]
$(Pb_{0.87}Ba_{0.1}La_{0.02})(Zr_{0.65}Sn_{0.3}Ti_{0.05})O_{3}$	73.0	[50]
$(Pb_{0.97}La_{0.02})(Zr_{0.58}Sn_{0.335}Ti_{0.085})O_{3}$	75.0	[51]
$Pb_{0.97}La_{0.02}(Zr_{0.58}Sn_{0.35}T_{0.07})O3$	86.1	[52]
$ (Pb_{0.99}Nb_{0.02})[(Zr_{0.57}Sn_{0.43})_{0.95}Ti_{0.05}]_{0.98}O_{3} \\$	65.0	[53]
(Pb _{0.88} La _{0.08})(Zr _{0.91} Ti _{0.09})O ₃	92.0	[22]
(Pb _{0.97} La _{0.02})(Zr _{0.95} Ti _{0.05})O ₃ + 10% PbO	93.0	[23]
Ag(Nb _{0.8} Ta _{0.2})O ₃	77.0	[54]
0.80NaNbO ₃ -0.20SrTiO ₃	80.7	[55]

5. Conclusions

Complex perovskites $Bi(Zn_{1/2}Ti_{1/2})O_3$, $Bi(Zn_{2/3}Nb_{1/3})O_3$, and $Bi(Zn_{3/4}W_{1/4})O_3$ are incorporated into PbZrO₃-based compositions to realize the relaxor antiferroelectric behavior for the purpose of enhancing the energy storage efficiency. It is found that $Bi(Zn_{2/3}Nb_{1/3})O_3$ is effective in introducing dielectric relaxation and diffuse transition, minimizing electric hysteresis,

and enhancing energy storage efficiency. In a model solid solution of $0.90(Pb_{0.97}La_{0.02})(Zr_{0.65}Sn_{0.30}Ti_{0.05})O_3-0.10Bi(Zn_{2/3}Nb_{1/3})O_3$, an electric hysteresis of 3.4 kV/cm, an energy storage density of 2.19 J/cm^3 , and an efficiency of 95.6% are demonstrated. Such a remarkable storage efficiency is the highest in antiferroelectric oxides ever reported in the literature.

Acknowledgements

The National Science Foundation (NSF), through Grant No. DMR-1700014, supported this work.

References

- [2] R. Xu, B. Li, J. Tian, Z. Xu, Y. Feng, X. Wei, D. Huang, L. Yang, Pb_{0.94}La_{0.04}[(Zr_{0.70}Sn_{0.30})_{0.90}Ti_{0.10}]O₃ antiferroelectric bulk ceramics for pulsed capacitors with high energy and power density, Appl. Phys. Lett. 110 (2017) 142904.
- [3] T. Kainz, B. Bitschnau, F.A. Mautner, K. Reichmann, Comparison of lanthanum and bismuth modification of lead zirconate-lead titanate PZT: A structural and dielectric study, J. Euro. Ceram. Soc. 36 (2016) 507–514.
- [4] P. Liu, M. Li, Q. Zhang, W. Li, Y. Zhang, M. Shen, S. Qiu, G. Zhang, S. Jiang, High thermal stability in PLZST antiferroelectric energy storage ceramics with the coexistence of tetragonal and orthorhombic phase, J. Euro. Ceram. Soc. 38 (2018) 5396–5401.
- [5] Z. Liu, T. Lu, J. Ye, G. Wang, X. Dong, R. Withers, Y. Liu, Antiferroelectrics for energy storage applications: A review, Adv. Mater. Technol. 3 (2018) 1800111.
- [6] H. Qi, R. Zuo, Evolving antiferroelectric stability and phase transition behavior in NaNbO₃–BaZrO₃–CaZrO₃ lead-free ceramics, J. Euro. Ceram. Soc. 39 (2019) 2318–2324.

^[1] A. Chauhan, S. Patel, R. Vaish, C.R. Bowen, Antiferroelectric ceramics for high energy density capacitors, Mater. 8 (2015) 8009-8031.

- [7] W.Y. Pan, C.Q. Dam, Q.M. Zhang, L.E. Cross, Large displacement transducers based on electric field forced phase transitions in the tetragonal (Pb_{0.97}La_{0.02})(Ti,Zr,Sn)O₃ family of ceramics, J. Appl. Phys. 66 (1989) 6014–6023.
- [8] O.E. Fesenko, R.V. Kolesova, Y.G. Sindeyev, Structural phase transitions in lead zirconate in super-high electric-fields, Ferroelectrics 20 (1978) 177–178.
- [9] D. Viehland, D. Forst, Z. Xu, J.F. Li, Incommensurately modulated polar structures in antiferroelectric Sn-modified lead zirconate titanate: the modulated structure and its influences on electrically induced polarizations and strains, J. Am. Ceram. Soc. 78 (1995) 2101–2112.
- [10] Z. Dai, Z. Xu, X. Yao, Effect of dc bias on pressure-induced depolarization of Pb(Nb,Zr,Sn,Ti)O₃ ceramics, Appl. Phys. Lett. 92 (2008) 072904.
- [11] P. Yang, D.A. Payne, Thermal stability of field-forced and field-assisted antiferroelectric-ferroelectric phase transformations in Pb(Zr,Sn,Ti)O₃, J. Appl. Phys. 71 (1992) 1361–1367.
- [12] H. He, X. Tan, Raman spectroscopy study of the phase transitions in Pb_{0.99}Nb_{0.02}[(Zr_{0.57}Sn_{0.43})_{1-y}Ti_y]_{0.98}O₃ ceramics, J. Phys.: Condens. Matter 19 (2007) 136003.
- [13] B.P. Pokharel, D. Pandey, Dielectric studies of phase transitions in (Pb_{1-x}Ba_x)ZrO₃, J. Appl. Phys. 88 (2000) 5364–5373.
- [14] M.J. Pan, S.E. Park, K.A. Markowski, W.S. Hackenberger, S. Yoshikawa, L.E. Cross, Electric field induced phase transition in lead lanthanum stannate zirconate titanate (PLSnZT) antiferroelectrics: Tailoring properties through compositional modification, Ferroelectrics 215 (1998) 153–167.
- [15] J. Wang, T. Yang, S. Chen, G. Li, High energy storage density performance of Ba, Sr-modified lead lanthanum zirconate titanate stannate antiferroelectric ceramics, Mater. Res. Bullet. 48 (2013) 3847–3849.
- [16] L.E. Cross, Relaxor ferroelectrics, Ferroelectrics 76 (1987) 241–267.
- [17] A. Bokov, Z.G. Ye, Recent progress in relaxor ferroelectrics with perovskite structure, J. Mater. Sci. 41 (2006) 31–52.
- [18] F. Li, S. Zhang, D. Damjanovic, L.Q. Chen, T.R. Shrout, Local structural heterogeneity and electromechanical responses of ferroelectrics: Learning from relaxor ferroelectrics, Adv. Funct. Mater. 28 (2018) 1801504.

- [19] C. Ma, X. Tan, Phase diagram of unpoled lead-free (1-x)(Bi_{1/2}Na_{1/2})TiO₃–xBaTiO₃ ceramics, Sol. St. Comm. 150 (2010) 1497–1500.
- [20] Y. Xu, H. Guo, X. Liu, Y. Feng, X. Tan, Effect of Ba content on the stress-sensitivity of the antiferroelectric to ferroelectric phase transition in (Pb,La,Ba,)(Zr,Sn,Ti)O₃ ceramics, J. Am. Ceram. Soc. 97 (2014) 206–212.
- [21] H. Borkar, V.N. Singh, B.P. Singh, M. Tomar, V. Gupta, A. Kumar, Room temperature lead-free relaxor-antiferroelectric electroceramics for energy storage applications, RSC Adv. 4 (2014) 22840–22847.
- [22] H.R. Jo, C.S. Lynch, A high energy density relaxor antiferroelectric pulsed capacitor dielectric, J. Appl. Phys. 119 (2016) 024104.
- [23] B. Li, Q.X. Liu, X.G. Tang, T.F. Zhang, Y.P. Jiang, W.H. Li, J. Luo, Antiferroelectric to relaxor ferroelectric phase transition in PbO modified (Pb_{0.97}La_{0.02})(Zr_{0.95}Ti_{0.05})O₃ ceramics with a large energy-density for dielectric energy storage, RSC Adv. 7 (2017) 43327–43333.
- [24] L. Jin, J. Pang, R. Jing, Y. Lan, L. Wang, F. Li, Q. Hu, H. Du, D. Guo, X. Wei, Z. Xu, L. Zhang, G. Liu, Ultra-slim pinched polarization-electric field hysteresis loops and thermally stable electrostrains in lead-free sodium bismuth titanate-based solid solutions, J. Alloys Comp. 788 (2019) 1182–1192.
- [25] K. Markowski, S.E. Park, S. Yoshikawa, L.E. Cross, Effect of compositional variations in the lead lanthanum zirconate stannate titanate system on electrical properties, J. Am. Ceram. Soc. 79 (1996) 3297–3304.
- [26] R. Seshadri, N.A. Hill, Visualizing the role of Bi 6s "lone pairs" in the off-center distortion in ferromagnetic BiMnO₃, Chem. Mater. 13 (2001) 2892–2899.
- [27] I. Grinberg, M.R. Suchomel, P.K. Davies, A.M. Rappe, Predicting morphotropic phase boundary locations and transition temperatures in Pb- and Bi-based perovskite solid solutions from crystal chemical data and first-principles calculations, J. Appl. Phys. 98 (2005) 094111.
- [28] M.R. Suchomel, P.K. Davies, Enhanced tetragonality in (x)PbTiO₃—(1-x)Bi(Zn_{1/2}Ti_{1/2})O₃ and related solid solution systems, Appl. Phys. Lett. 86 (2005) 262905.
- [29] O. Khamman, X. Tan, S. Ananta, R. Yimnirun, Ferroelectric properties of (1-x)Bi(Zn_{1/2}Ti_{1/2})O₃-xPbZrO₃ ceramics, J. Mater. Sci. 44 (2009) 4321–4325.
- [30] D.M. Stein, M.R. Suchomel, P.K. Davies, Enhanced tetragonality in (x)PbTiO₃–(1-x)Bi(B'B")O₃ systems: Bi(Zn_{3/4}W_{1/4})O₃, Appl. Phys. Lett. 89 (2006) 132907.

- [31] C.C. Huang, D.P. Cann, Phase transitions and dielectric properties in Bi(Zn_{1/2}Ti_{1/2})O₃–BaTiO₃ perovskite solid solutions, J. Appl. Phys. 104 (2008) 024117.
- [32] A. Paterson, H.T. Wong, Z. Liu, W. Ren, Z.G. Ye, Synthesis, structure and electric properties of a new lead-free ferroelectric solid solution of (1-x)BaTiO₃–xBi(Zn_{2/3}Nb_{1/3})O₃, Ceram. Int. 41 (2015) S57–S62.
- [33] X. Chen, J. Chen, D. Ma, H. Zhou, L. Fang, Thermally stable BaTiO₃–Bi(Zn_{0.75}W_{0.25})O₃ solid solution with high relative permittivity and low dielectric loss, J. Mater. Sci.: Mater. Electron. 26 (2015) 1413–1418.
- [34] Z. Liu, H. Wu, A. Paterson, W. Ren, Z.G. Ye, Effects of Bi(Zn_{2/3}Nb_{1/3})O₃ modification on the relaxor behavior and piezoelectricity of Pb(Mg_{1/3}Nb_{2/3})O₃–PbTiO₃ ceramics, IEEE Trans. Ultrason. Ferroelectr. Freq. Contr. 64 (2017) 1608–1616.
- [35] R.D. Shannon, Revised effective ionic radii and systematic studies of interatomic distances in halides and chalcogenides, Acta Cryst. A32 (1976) 751–767.
- [36] M. Chen, X. Yao, L. Zhang, Grain size dependence of dielectric and field-induced strain properties of chemical prepared (Pb, La)(Zr, Sn, Ti)O₃ antiferroelectric ceramics, Ceram. Int. 28 (2002) 201–207.
- [37] Z. Fan, F. Xue, G. Tutuncu, L.Q. Chen, X. Tan, Interaction dynamics between ferroelectric and antiferroelectric domains in a PbZrO₃-based ceramic, Phys. Rev. Appl. 11 (2019) 064050.
- [38] D. Viehland, D. Forst, J.F. Li, Compositional heterogeneity and the origins of the multicell cubic state in Sn-doped lead zirconate titanate ceramics, J. Appl. Phys. 75 (1994) 4137–4143.
- [39] U. Sukkha, N. Vittayakorn, R. Guo, A.S. Bhalla, Phase transition behavior of Ba(Mg_{1/3}Nb_{2/3})O₃ modified PbZrO₃ solid solution, J. Mater. Chem. C 2 (2014) 2929–2938.
- [40] H. Shimizu, H. Guo, S.E. Reyes-Lillo, Y. Mizuno, K.M. Rabe, C.A. Randall, Lead-free antiferroelectric: xCaZrO₃–(1-x)NaNbO₃ system (0 ≤ x ≤ 0.10), Dalton Trans. 44 (2015) 10763–10772.
- [41] H. Guo, H. Shimizu, Y. Mizuno, C.A. Randall, Strategy for stabilization of the antiferroelectric phase (*Pbma*) over the metastable ferroelectric phase (*P2₁ma*) to establish double loop hysteresis in lead-free (1-x)NaNbO₃–xSrZrO₃ solid solution, J. Appl. Phys. 117 (2015) 214103.

- [42] L. Pauling, The Nature of the Chemical Bond, 3rd ed., Cornell Univ. Press, New York, 1960.
- [43] X. Zhao, W. Qu, X. Tan, Zr-modified Pb(Mg_{1/3}Nb_{2/3})O₃ with long range cation order, J. Am. Ceram. Soc. 91 (2008) 3031–3038.
- [44] H.T. Martirena, J.C. Burfoot, Grain-size and pressure effects on dielectric and piezoelectric properties of hot-pressed PZT-5, Ferroelectrics 7 (1974) 151–152.
- [45] K. Uchino, S. Nomura, Critical exponents of the dielectric-constants in diffused phase transition crystals, Ferroelectrics Lett. Sect. 44 (1982) 55–61.
- [46] N. Vittayakorn, G. Rujijanagul, X. Tan, M.A. Marquardt, D.P. Cann, The morphotropic phase boundary and dielectric properties of the xPb(Zr_{1/2}Ti_{1/2})O₃–(1-x)Pb(Ni_{1/3}Nb_{2/3})O₃ perovskite solid solution, J. Appl. Phys. 96 (2004) 5103–5109.
- [47] J. Cui, Y.S. Chu, O.O. Famodu, Y. Furuya, J. Hattrick-Simpers, R.D. James, A. Ludwig, S. Thienhaus, M. Wuttig, Z. Zhang, I. Takeuchi, Combinatorial search of thermoelastic shapememory alloys with extremely small hysteresis width, Nat. Mater. 5 (2006) 286–290.
- [48] X. Yang, F. Zhuo, C. Wang, Y. Liu, Z. Wang, H. Tailor, C. He, X. Long, High energy storage density and ultrafast discharge in lead lutetium niobate based ceramics, J. Mater. Chem. A 7 (2019) 8414–8422.
- [49] I.V. Ciuchi, L. Mitoseriu, C. Galassi, Antiferroelectric to ferroelectric crossover and energy storage properties of $(Pb_{1-x}La_x)(Zr_{0.90}Ti_{0.10})_{1-x/4}O_3$ $(0.02 \le x \le 0.04)$ ceramics, J. Am. Ceram. Soc. 99 (2016) 2382–2387.
- [50] S. Jiang, L. Zhang, G. Zhang, S. Liu, J. Yi, X. Xiong, Y. Yu, J. He, Y. Zeng, Effect of Zr:Sn ratio in the lead lanthanum zirconate stannate titanate antiferroelectric ceramics on energy storage properties, Ceram. Int. 39 (2013) 5571–5575.
- [51] Z. Liu, X. Chen, W. Peng, C. Xu, X. Dong, F. Cao, G. Wang, Temperature-dependent stability of energy storage properties of Pb_{0.97}La_{0.02}(Zr_{0.58}Sn_{0.335}Ti_{0.085})O₃ antiferroelectric ceramics for pulse power capacitors, Appl. Phys. Lett. 106 (2015) 262901.
- [52] X. Song, Y. Zhang, Y. Chen, Q. Zhang, J. Zhu, D. Yang, Effect of titanium content on dielectric and energy storage properties of (Pb,La,Sr)(Zr,Sn,Ti)O₃ ceramics, J. Electron. Mater. 44 (2015) 4819–4824.
- [53] S.E. Young, J.Y. Zhang, W. Hong, X. Tan, Mechanical self-confinement to enhance energy storage density of antiferroelectric capacitors, J. Appl. Phys. 113 (2013) 054101.

- [54] L. Zhao, Q. Liu, J. Gao, S. Zhang, J.F. Li, Lead-free antiferroelectric silver niobate tantalate with high energy storage performance, Adv. Mater. 29 (2017) 1701824.
- [55] M. Zhou, R. Liang, Z. Zhou, S. Yan, X. Dong, Novel sodium niobate-based lead-free ceramics as new environment-friendly energy storage materials with high energy density, high power density, and excellent stability, ACS Sustainable Chem. Eng. 6 (2018) 12755– 12765.